Topographic Influence on Baroclinic Instability and the Mesoscale Eddy Field in the Northern North Atlantic Ocean and the Nordic Seas

MARTA TRODAHL

University of Oslo, Oslo, Norway

PÅL ERIK ISACHSEN

University of Oslo, and Norwegian Meteorological Institute, Oslo, Norway

(Manuscript received 24 October 2017, in final form 3 September 2018)

ABSTRACT

A weak planetary vorticity gradient and weak density stratification in the northern North Atlantic and Nordic seas lead to time-mean currents that are strongly guided by bottom topography. The topographic steering sets up distinct boundary currents with strong property fronts that are prone to both baroclinic and barotropic instability. These instability processes generate a macroturbulent eddy field that spreads buoyancy and other tracers out from the boundary currents and into the deep basins. In this paper we investigate the particular role played by baroclinic instability in generating the observed eddy field, comparing predictions from linear stability calculations with diagnostics from a nonlinear eddy-permitting ocean model hindcast. We also look into how the bottom topography impacts instability itself. The calculations suggest that baroclinic instability is a consistent source of the eddy field but that topographic potential vorticity gradients impact unstable growth significantly. We also observe systematic topographic effects on finite-amplitude eddy characteristics, including a general suppression of length scales over the continental slopes. Investigation of the vertical structure of unstable modes reveal that Eady theory, even when modified to account for a bottom slope, is unfit as a lowest-order model for the dynamics taking place in these ocean regions.

1. Introduction

The northwestern North Atlantic Ocean and Nordic seas are probably the places in the world where bottom topography has its biggest impact on the ambient potential vorticity (PV) gradients that govern large-scale ocean flows. The reason is a combination of a weak planetary vorticity gradient and a weak density stratification caused by persistent air–sea cooling. The planetary vorticity gradient in the Arctic Ocean is even weaker, but there the water column is more strongly stratified because of the large influx of river water and the distillation process caused by the seasonal cycle of sea ice freezing and melting. So it is in the northern North Atlantic and in the sub-Arctic that topographic effects are most dramatic.

The strong topographic steering in these regions can be seen in the top panel of Fig. 1. Shown are observed time-mean sea surface temperatures (SST) extracted from the Operational Sea Surface Temperature and Sea Ice Analysis (OSTIA) reanalysis (Donlon et al. 2012) as well as time-mean geostrophic surface currents estimated by differentiating the mean dynamic topography (MDT) distributed by AVISO. In the Nordic seas, observations like these have inspired lowest-order descriptions of the large-scale flow fields based on closed f/H theory (Nøst and Isachsen 2003; Isachsen et al. 2003; Aaboe and Nøst 2008) where currents, at least at the bottom, are assumed to essentially follow f/H contours (f is the Coriolis parameter and H is the bottom depth). Where such contours close on themselves, as they do in ocean basins where gradients in H dominate over gradients in f, the theories predict circulation strengths from approximate balances between divergences in the top and bottom Ekman layers. Similar descriptions of large-scale balances in the Irminger and Labrador Seas of the northwestern North Atlantic are still missing, but Fig. 1 makes it evident that topography plays a lowest-order role there too. Currents also feel the bottom in the eastern North Atlantic but to a lesser degree because of a stronger vertical density stratification there.

Corresponding author: Marta Trodahl, marta.trodahl@geo.uio.no

DOI: 10.1175/JPO-D-17-0220.1

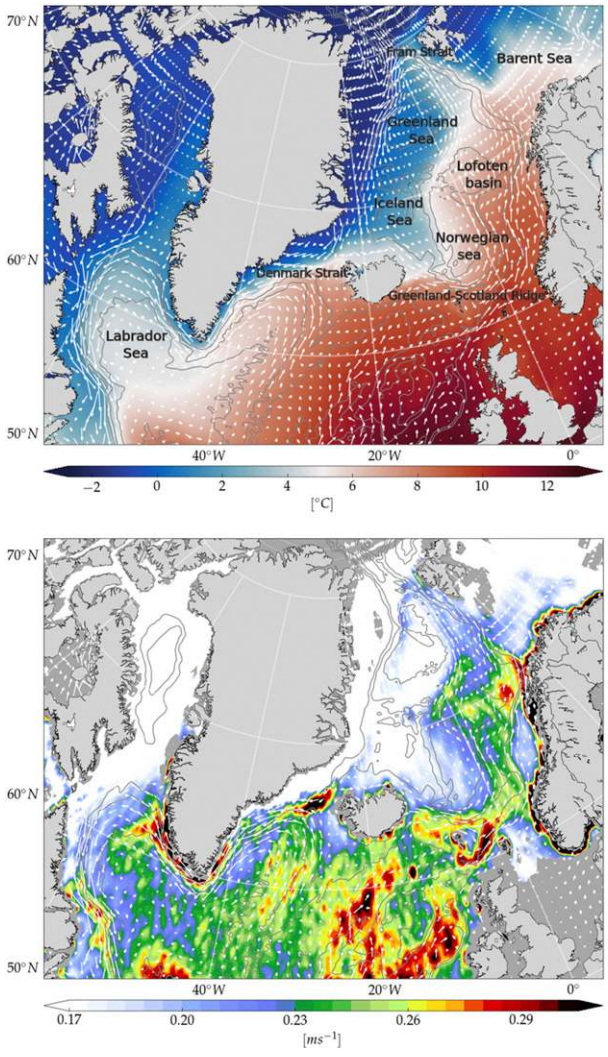

FIG. 1. (top) Time-mean sea surface temperatures (°C) from the OSTIA reanalysis and (bottom) square root of geostrophic EKE ($m\,s^{-1}$) obtained by differentiating along-track SSH anomalies provided by AVISO. Vectors show time-mean surface geostrophic currents (arbitrary scale), also provided by AVISO.

The strong topographic steering in the west and the north creates distinct property fronts, especially between poleward-flowing warm and salty Atlantic Water (AW) and southward-flowing cold and fresh Polar Water (PW). The sharpness of these fronts must somehow reflect a balance between alongfront advection by the time-mean currents and across-front stirring or ''mixing'' by mesoscale or submesoscale transients. And, unsurprisingly, most of the frontal zones are also associated with high flow variability, as illustrated by an estimate of surface eddy kinetic energy (EKE) given in the bottom panel of Fig. 1. So the large-scale currents clearly feel the topography, hence the sharp fronts. But to what extent is this also the case for the instability processes and mesoscale eddy field whose raison d'être is to wash out those same fronts?

Studies of the stability of large-scale currents and on mesoscale dynamics in the northwestern North Atlantic and Nordic seas have mostly focused on energetic hot spots like the Labrador Sea and the Lofoten Basin of the Nordic seas. Several studies have suggested that Labrador Sea eddies can be categorized into at least two groups: Irminger rings (IR) and boundary current eddies (BCEs) (Chanut et al. 2008; Gelderloos et al. 2011; Hátún et al. 2007). The IRs are long lived, primarily warm anticyclonic eddies formed in the region off Cape Desolation, whereas the smaller BCEs are fresh and form all along the boundary current. (Lilly et al. 2003; Gelderloos et al. 2011; de Jong et al. 2014; Hátún et al. 2007). The sources of these vortices have been studied both with primitive equation models of varying levels of realism (Eden and Böning 2002; Katsman et al. 2004; Chanut et al. 2008) and with idealized quasigeostrophic models (Bracco and Pedlosky 2003; Bracco et al. 2008). The more realistic model studies suggested that both baroclinic and barotropic, or even mixed instability, may be present whereas the idealized QG studies indicated that baroclinic instability alone was sufficient at explaining both the spatial distribution and scales of much of the observed eddy field. Topographic influence was predominant in all studies, and Bracco and Pedlosky (2003) and Bracco et al. (2008) found that baroclinic instability, in particular, is suppressed by the topographic PV gradient associated with the continental slope. But the same authors also found that the flow would get extremely unstable along a particularly steep part of the slope. This interesting result is in agreement with the observations in Fig. 1 that show enhanced mesoscale eddy activity off the steepest part of the southern Greenland slope.

In the Nordic seas, linear baroclinic instability of the Norwegian Atlantic Current (NwAC) as it skirts the Lofoten Basin off northern Norway was studied by Isachsen (2015). Quasigeostrophic (QG) vertical mode calculations carried out on the background state of a model with realistic bathymetry suggested that the flow there is also most unstable over the steepest part of the continental slope, in agreement with the findings from the Labrador Sea. This behavior is not obvious. In classical Eady theory (where the planetary vorticity gradient, relative vorticity, and variations in layer thickness are all neglected) instability forms by an interaction between top and bottom edge waves. Eady or two-layer Phillips theory can be modified to take a linear bottom slope into account (Blumsack and Gierasch 1972; Mechoso 1980; Isachsen 2011). The modified theory generally suggests *suppressed* growth

over an inclined bottom—relative to growth over a flat bottom. Stability is controlled by the slope parameter $\delta = \alpha/s$, where α is the bottom slope and s is the isopycnal slope. In the boundary currents present in our study region, with buoyant surface currents flowing with the coast to their right, δ is negative. For such a setting, modified Eady theory predicts both lower growth rates and smaller scales compared to flat-bottom conditions. The following question then emerges: How does one reconcile this prediction with the indication in Fig. 1 that eddy activity is *enhanced* along the steeper parts of the continental slopes in both the Labrador Sea and Nordic seas?

Bracco and Pedlosky (2003) and Bracco et al. (2008) explained the faster growth along very steep continental slopes by considering the dynamics of a current stabilized by topography everywhere except for a small region that has infinite slope (i.e., a vertical wall). But Isachsen (2015) obtained the highest growth rates over the steepest part of the slope without resorting to such a limiting case. Inspection of the vertical structure of unstable waves instead revealed that Eady or two-layer Phillips instability is typically not at play. The bottom topography basically changes the near-bottom PV gradient to the extent that interaction between surface and bottom edge waves is prohibited. Instead, unstable growth in the QG model occurs by interactions between edge waves at either the top or bottom surfaces and interior ''Rossby'' or PV waves existing because of layer thickness gradients. Or, in some cases, instability is caused by interactions entirely between interior PV waves.

Regardless of the details, the isolated studies from both the Labrador Sea and the Lofoten Basin have suggested that bottom topography may have a lowest-order effect on baroclinic instability of the cyclonic boundary currents that characterize the large-scale flow in these ocean regions. The purpose of the present study is to extend the investigation of topographic effects on baroclinic instability to the entire northern North Atlantic and Nordic seas. We will repeat the QG modal analysis of Isachsen (2015) and look into the PV dynamics that impacts the most unstable waves in different regions. The questions we raise are, first, whether baroclinic instability may be the main source of the observed mesoscale eddy variability in the region; second, whether the Eady model gives a useful quantitative description of growth rates and length scales; and third, what more general QG dynamics can reveal about topographic control on unstable growth.

We will do the linear stability calculations using time-mean fields of an eddy-permitting regional ocean model rather than on gridded observed fields. The reason behind this choice is a strong sensitivity of growth to the alignment of background currents relative to topographic gradients. A proper alignment is hard to obtain from, say, gridded hydrography (for the thermal wind shear) combined with gridded altimeter fields (for surface reference-level velocities). Analyzing fields from an eddy-permitting model also allows for an assessment of the relevance of linear theory in explaining the geographic distribution of the fully developed mesoscale eddy field in the same model.

In the following we present the model dataset and give an overview of methods used for analysis. We then show the results, first by characterizing the strength and lateral scales of the eddy field in the nonlinear ocean model. Energy conversion rates that indicate where both baroclinic and barotropic instability take place are also presented. Then we present results from the linear stability calculations and compare growth rates and corresponding lateral scales to the eddy characteristics from the nonlinear field. A comparison with the standard Eady prediction is also made. Finally, the vertical structure of unstable waves and its relation to topographic effects and the background PV gradients are studied at a few key locations. The paper ends with a summary and discussion of our results.

2. Data and methods

a. *Model simulations*

The ''data'' for our study comes from a 17-yr-long eddy-permitting ocean model simulation conducted with the Regional Ocean Modeling System (ROMS; Shchepetkin and McWilliams 2005; Haidvogel et al. 2008) coupled to a sea ice module. ROMS is a hydrostatic, primitive equation model formulated with a near-orthogonal staggered C-grid in the horizontal and a vertical s-coordinate system in which the layers are draped over the seabed terrain. The s-coordinate is a generalized sigma coordinate, amended to allow for a more flexible vertical distribution of the layers.

The model's lateral grid spacing is 4 km. This resolution is sufficient to support the presence of mesoscale eddies on the scale of the internal Rossby deformation radius throughout most of the domain except for over very shallow shelf regions. The vertical grid consists of 35 layers distributed to obtain a finer resolution near the surface. A fourth-order centered scheme is used for vertical advection and a third-order upwind scheme is used for horizontal tracer and momentum advection. No explicit horizontal eddy viscosity or diffusion is applied, but the upwind advection scheme includes some implicit biharmonic diffusion. The *k*–epsilon version of the general

length scale (GLS) scheme (Umlauf and Burchard 2003; Warner et al. 2005) is employed for small-scale vertical mixing. The open lateral boundaries are relaxed toward the Global Forecast Ocean Assimilation Model (FOAM; MacLachlan et al. 2015), and atmospheric forcing is attained from the ERA-Interim atmospheric reanalysis (Uppala et al. 2005).

For all the analysis below we use daily mean fields. Hence, tides and other motions excited by fast atmospheric forcing have been filtered out. Such filtering should be justified given the focus on ocean mesoscale processes that typically have time scales from a few days to several weeks or months. We analyze only the last 10 years of the model simulation (1999–2009) to ensure that the dynamics has spun up to be consistent with boundary conditions.

The model time-mean SST and surface flow field are shown in Fig. 2. The model contains finer structure than what is seen in the observations, reflecting a coarser effective resolution in the observational dataset. But the general structure of the two fields agree well, and the model captures all the major frontal zones. Some of the AW, which should have entered the Nordic seas via the Denmark Strait between Iceland and Greenland instead recirculates there and is then transported by the East Greenland Current (EGC) into the Labrador Sea. Recirculation also happens in reality but appears to be stronger in the model, resulting in a Labrador Sea that is slightly too warm. In the northeastern Nordic seas the shelf regions are also slightly too warm and the deep basins too cold. This might indicate that the model currents are too constrained by topography, an effect not uncommon in models with terrain-following vertical coordinate systems (Haney 1991).

The figure also shows the model time-mean surface EKE field averaged over the 10-yr diagnostics period. Here we have used the definition $\mathrm{EKE} = (\overline{u'^2} + \overline{v'^2})/2$, where u and v are surface velocity components, the overlines represent means over time scales from one day to three months, and the primes indicate anomalies from such means. For EKE too, the more refined structures in the model field reflect a higher resolution compared to the observations. Note that the altimeter data contain instrumental noise that produces artificially high EKE levels at high wavenumbers (Le Traon et al. 1990). This is likely responsible for a general higher EKE level in the observations compared to the model, as seen especially in relatively quiescent regions. But the main spatial patterns of variability are captured in the model, including the tongue extending from the steep region off Greenland's southwestern coast. Model EKE levels in the Lofoten Basin are lower than in observations whereas EKE over the main boundary current there is higher. This might again reflect an overly strong topographic steering in the model.

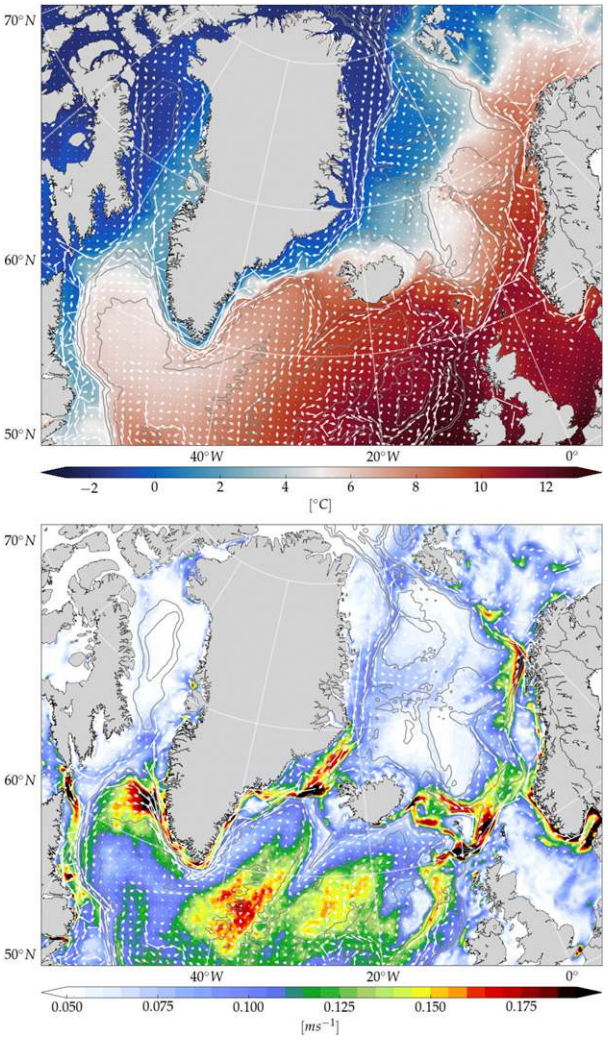

FIG. 2. (top) Model time-mean (1999–2009) SST (°C) and (bottom) square root of surface EKE ($\mathrm{m\,s^{-1}}$).

b. Eddy detection

Coherent mesoscale eddies were identified in the fully turbulent model run by the hybrid method of Penven et al. (2005). This involves locating closed contours of both SSH (streamlines for the surface geostrophic flow when the Rossby number is small) and the Okubo–Weiss (OW) parameter. The OW parameter is a measure of the relative strength of vorticity versus deformation, taking the following form:

$$\mathrm{OW} = S_n^2 + S_s^2 - \zeta^2,$$

where the normal strain $S_n = \partial_x u - \partial_y v$ and shear strain $S_s = \partial_x v + \partial_y u$ represent the total deformation while

relative vorticity $\zeta = \partial_x v - \partial_y u$ represents rotation. So, essentially, regions in the flow field having OW $\lesssim 0$ potentially indicate the core of coherent eddies (where rotation is expected to dominate over deformation). Although the OW parameter is originally designed to identify coherent structures in idealized 2D turbulent flows, it is also a commonly used tool for identifying vortices in real geophysical flows (Isern-Fontanet et al. 2003; Penven et al. 2005; Chelton et al. 2007).

For daily averaged model fields at 4-km horizontal resolution, we can expect both temporal and advective Rossby numbers (assuming flow speeds up to 0.5 m s^{-1}) to be well below one. So closed SSH contours are also good indicators of closed geostrophic streamlines. For each daily model field, local SSH extrema were thus identified and required to hold within a square of 24 neighboring grid points. This ensures a lower limit on the separation distance between two adjacent eddies, and overestimated eddy counts are more likely avoided as smaller variations in the SSH field are ignored. Within each such closed SSH region the OW parameter was then calculated from depth-averaged horizontal velocities. Where negative OW values were found, the edge of an eddy was defined by the OW = 0 contour.

For each detected eddy, a characteristic eddy kinetic energy and eddy effective radius were calculated from

$$\mathrm{EKE} = \frac{1}{A}\int\int \frac{u'^2 + v'^2}{2} dA,$$

$$R = \sqrt{\frac{A}{\pi}},$$

where A is the area of the eddy (the region within the OW = 0 contour). Finally, with the finite resolution of the model in mind, a minimum eddy effective radius was set to 8 km. Features smaller than this were rejected. Also, a maximum eddy radius was set to 200 km to prevent an entire ocean gyre to be identified as an eddy.

c. *Linear stability calculations*

Linear baroclinic instability of the time-mean field in the model was studied using the algorithm proposed by Smith (2007). The basis for the analysis is the QG tendency equations for perturbation PV and buoyancy. The equations are linearized about a horizontally homogeneous mean state that consists of a background horizontal flow $\mathbf{U}(z) = U\hat{\mathbf{i}} + V\hat{\mathbf{j}}$ and vertical stratification $N^2(z) = -g/\rho_0 \partial_z \rho$ (where g is the gravitational acceleration, ρ is the background potential density field, and ρ_0 is a reference density). For small perturbations this gives

$$(\partial_t + \mathbf{U}\cdot\nabla)q + \mathbf{u}\cdot\nabla Q = 0, \quad -H < z < 0, \tag{1}$$

$$(\partial_t + \mathbf{U}\cdot\nabla)b + \mathbf{u}\cdot\nabla B = 0, \quad z = 0, \quad \text{and} \tag{2}$$

$$(\partial_t + \mathbf{U}\cdot\nabla)b + \mathbf{u}\cdot\nabla B + N^2\mathbf{u}\cdot\nabla h = 0, \quad z = -H, \tag{3}$$

where Q and B are the background potential vorticity and buoyancy, respectively; and q and b are the corresponding perturbations. The term $\mathbf{u}(z) = u\hat{\mathbf{i}} + v\hat{\mathbf{j}}$ is the perturbation horizontal velocity, and h is the bottom topography variation, assumed to be small compared to total depth H. Note that ∇ is the horizontal gradient operator.

In terms of the geostrophic streamfunction $\psi = p/(\rho_0 f)$ (p is pressure and f is the Coriolis parameter), the horizontal velocity is $\mathbf{u} = \hat{\mathbf{k}} \times \nabla\psi$, and the vertical component of relative vorticity is $\zeta = \nabla^2\psi$. Further we get that

$$Q = \nabla^2\Psi + \beta y + \Gamma\Psi,$$

$$q = \nabla^2\psi + \Gamma\psi,$$

$$B = f_0 \partial_z \Psi,$$

$$b = f_0 \partial_z \psi,$$

where upper- and lowercase letters denote mean and perturbation terms; f_0 and βy are the constant and variable parts of the planetary vorticity, respectively; and $\Gamma = \partial_z[(f_0^2/N^2)\partial_z]$ is the so-called stretching operator that represents QG isopycnal layer thickness.

We assume a plane-wave solution, $\psi = \Re[\hat{\psi}(z)e^{i(kx+ly-\omega t)}]$, where $\hat{\psi}$ is the vertical structure of the perturbation, ω is the wave frequency, and k, l are horizontal wavenumbers. Under the local approximation, in which we assume a horizontally slowly varying background field, we ignore the mean relative vorticity $\nabla^2\Psi$. Substitution into the evolution equations gives the following:

$$\omega(\Gamma - \kappa^2)\hat{\psi} = [\mathbf{K}\cdot(\hat{\mathbf{k}}\times\nabla Q) + \mathbf{K}\cdot\mathbf{U}(\Gamma - \kappa^2)]\hat{\psi}, \quad -H < z < 0, \tag{4}$$

$$(\mathbf{K}\cdot\mathbf{U} - \omega)\partial_z\hat{\psi} = \mathbf{K}\cdot\partial_z\mathbf{U}, \quad z = 0, \quad \text{and} \tag{5}$$

$$(\mathbf{K}\cdot\mathbf{U} - \omega)\partial_z\hat{\psi} = \mathbf{K}\cdot\Omega\hat{\psi}, \quad z = -H. \tag{6}$$

Here $\mathbf{K} = k\hat{\mathbf{i}} + l\hat{\mathbf{j}}$ is the horizontal wave vector, and $\kappa = \sqrt{k^2 + l^2}$ is its modulus. Finally, $\Omega = (\partial_z U - N^2/f_0\partial_y h)\hat{\mathbf{i}} + (\partial_z V + N^2/f_0\partial_x h)\hat{\mathbf{j}}$.

The analysis amounts to solving a generalized eigenvalue problem in discrete form is

$$\omega\mathbf{B}_{ij}\hat{\boldsymbol{\psi}}_j = \mathbf{A}_{ij}\hat{\boldsymbol{\psi}}_j. \tag{7}$$

Here **A** and **B** are tridiagonal, asymmetric (35×35) matrices containing the terms

$$\mathbf{B}_{ij} = \mathbf{\Gamma}_{ij} - K^2 \boldsymbol{\delta}_{ij}, \tag{8}$$

$$\mathbf{A}_{ij} = (k\mathbf{Q}_y^m - l\mathbf{Q}_x^m)\boldsymbol{\delta}_{ijm} + (k\mathbf{U}^m + l\mathbf{V}^m)\boldsymbol{\delta}_{inm}\mathbf{B}_{nj}, \tag{9}$$

where i, j index the rows and columns. The δ symbols represent Kronecker tensors,

$$\boldsymbol{\delta} = \begin{cases} 0, & i \neq n \neq m \\ 1, & i = n = m \end{cases}, \tag{10}$$

with the value 1 on the diagonal elements, and otherwise zero. Hence the tensor products with $\boldsymbol{\delta}_{ijm}$, $\boldsymbol{\delta}_{inm}$, in $\mathbf{A}_{ij}$, leaves matrices with $(kQ_{y,i} - lQ_{x,i})$ and $(kU_i + lV_i)$ on the diagonals.

The eigenvalue problem is discretized on the staggered vertical model grid [see appendix B in Smith (2007)]. The discretized problem is solved at every horizontal model grid point for 200×200 wavenumbers. With Eady dynamics in mind, where the fastest-growing wave has a scale near the internal deformation radius, we calculated growth in the wavenumber range $0.1k_d < |k, l| < 10k_d$, where $k_d = 1/L_d$, and L_d is the internal deformation radius, approximated by its WKB expression:

$$L_d = \frac{1}{f}\int_{-H}^{0} N\, dz. \tag{11}$$

Since the model has 35 vertical levels we get, at each location, 35 eigenvectors and their associated eigenvalues. The eigenvalues are complex ($\omega = \omega_r + i\omega_i$), and positive imaginary components give modes that grow exponentially in time.

In some cases, the waves selected by the above algorithm represent very small-scale surface or bottom intensified instabilities. Smith (2007) argues that such instabilities are likely of less significance in the extraction of available potential energy (APE) from the mean flow. Smith applied a filter in the selection process based on a measure of the waves' ability to extract mean-flow APE, in order to weed out the less important features. Here we instead followed the procedure of Vollmer and Eden (2013) and use a scale-selective horizontal diffusion operator, by adding $A_h\nabla^2 q$ to the right-hand side of Eq. (1) with $A_h = 10\,\mathrm{m^2\,s^{-1}}$, to filter out the smallest-scale perturbations. We are still not guaranteed the most energetically important perturbation by simply choosing the wave corresponding to the global maximum growth rate; however, we are now somewhat more liable to select a larger, possibly deeper, mode.

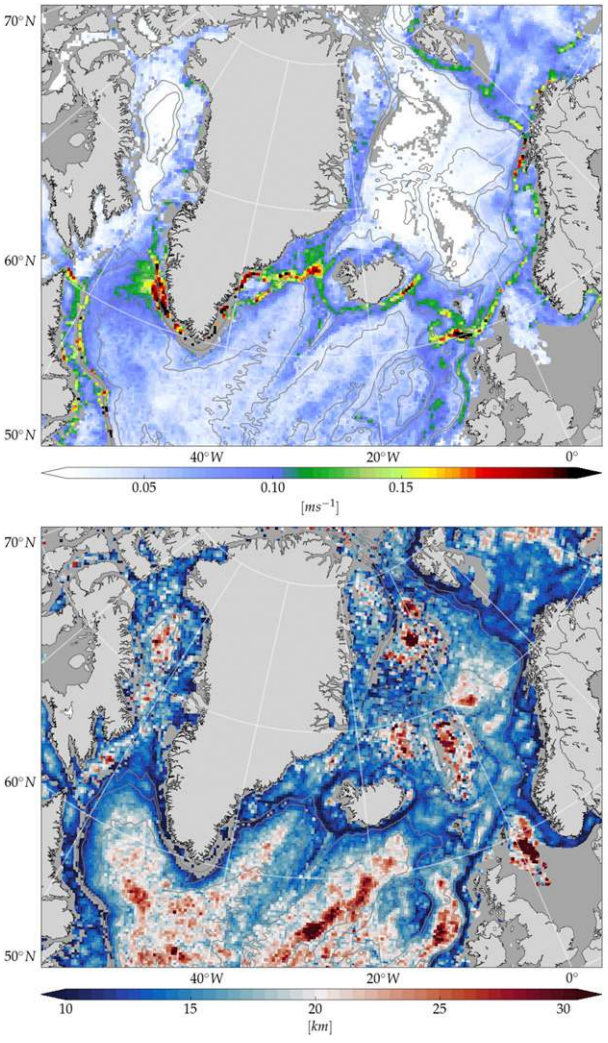

FIG. 3. Characteristics of detected coherent vortices: (top) square root of EKE ($\mathrm{m\,s^{-1}}$) and (bottom) effective radius (km). Gray regions indicate where no coherent eddies were detected or where the depth is shallower than 100 m.

3. Results

a. Characteristics of the fully developed eddy field

Figures 1 and 2 show that the topographically guided boundary currents are also regions of high EKE, at least at the surface. But EKE estimates like these, made from a simple band passing of the velocity field, do not distinguish between macroturbulence created by instability and other types of variability reflecting, say, meandering of the currents or modulation of the current strengths. To start assessing whether the high EKE levels are indeed related to active instability processes, we will therefore look at actual eddies—coherent vortices—detected from the model field. The characteristic EKE and radius of the detected eddies are shown in Fig. 3.

The estimates have been averaged over the entire 10-yr run and over 20 km × 20 km boxes. A quantitative comparison with the Reynolds EKE in Fig. 2 would require a consideration of the eddy density (i.e., the frequency of vortex detections in each region). We do not pursue this but note that the overall vortex EKE pattern is in good general agreement with the Reynolds EKE. Some of the elevated Reynolds EKE levels over the deep basins of the northeastern North Atlantic do not have corresponding high vortex EKE. Presumably, variability there is instead reflecting variable wind forcing over this main storm-track corridor. But the comparison suggests that high EKE levels along all major frontal zones over continental slopes and underwater ridge systems reflects an abundance of coherent eddies and not just modulation of the strength and position of the currents.

There are regions in the model where absolutely no coherent eddies were found by the detection algorithm. In the Norwegian and Greenland basins as well as the Icelandic Plateau Reynolds EKE levels are extremely low (see also Figs. 1 and 2), so these are simply relatively quiescent regions. More conspicuous is an apparent lack of detected eddies along the southern tip of Greenland and along the continental slope of the southwestern Labrador Sea. The slope region off the southern tip of Greenland is otherwise characterized by high Reynolds EKE levels (see also Fig. 2), so this particular result is counter to expectations. But a probable explanation for the apparent lack of coherent vortices here is hinted at by our estimate of eddy effective radius shown in the bottom panel of Fig. 3. The estimate reveals that coherent eddies along the continental slope off southern Greenland are very small, near the vortex detection threshold, which we have set to 8 km.

The figure also shows a more interesting *general* tendency of reduced eddy length scales over nearly all the continental slopes. So the main frontal zones that contain the highest EKE levels are, at the same time, associated with smaller eddy scales. Suppressed length scales over topographic slopes may be associated with a halted inverse energy cascade caused by topographic Rossby wave radiation (Vallis and Maltrud 1994; LaCasce and Brink 2000). But, as mentioned in the introduction, suppressed scales over sloping bottoms is also consistent with the linearized baroclinic instability theory of Blumsack and Gierasch (1972).

The actual predictions of linearized theory in this region will be studied below. But before that we look briefly into the energetics of the fully developed macroturbulent field in the model. The conversion terms from mean flow energy to eddy available potential energy (EAPE) and to EKE are, respectively (Eden and Böning 2002),

$$T_2 = \int_{-H}^{0} -\rho_0 \overline{\mathbf{u}'b'} \cdot \frac{\nabla \overline{b}}{N^2}\, dz, \tag{12}$$

and

$$T_4 = \int_{-H}^{0} -\rho_0 \overline{\mathbf{u}'\mathbf{u}'} \cdot \nabla \overline{\mathbf{u}}\, dz. \tag{13}$$

In our diagnosis of these terms from model fields the overbars and primes represent the same time means and perturbations that we have earlier used to diagnose Reynolds EKE. Here N^2 is the horizontally local time-mean buoyancy frequency. Most other studies have used some form of globally averaged N^2 in their definition of APE and hence in estimating T_2 (e.g., Chen et al. 2014; Zhu et al. 2014; Eden and Böning 2002; Aiki et al. 2016; von Storch et al. 2012). But since there will always be an element of arbitrariness in the exact definition of APE, and since our discussion here will primarily be qualitative, we simply use the local value of N^2.

Our estimate of the "baroclinic production" term T_2 (related to baroclinic instability) shown in the top panel of Fig. 4, reveals positive values practically everywhere. In the energy framework of Lorenz (1955), this is consistent with the energy flow path of baroclinic instability. The production of EAPE primarily takes place along the major boundary currents and frontal zones, and this is much as expected. The agreement with model EKE (Figs. 2 and 3) is good but far from perfect. One reason for the discrepancy is that the connection between EAPE and EKE goes via a vertical Reynolds flux $\overline{w'b'}$. We do not show this term here, but it reveals the EAPE → EKE transfer, which is also enhanced over the boundary currents. More important is the fact that the equlilibrated EKE field reflects not only a balance between local production and dissipation but also the transport convergence of EKE by both the mean flow and the turbulent field itself. There are multiple indications of mean flow EKE advection that lead to enhanced EKE levels downstream of T_2 maxima (e.g., as seen both along the southwestern Greenland coast and north Norwegian coast). And enhanced EKE levels extending into the deep Labrador and Lofoten basins likely indicate that eddies act to spread EKE across the continental slopes. Finally, there are some instances of large positive T_2 values with little correspondence in elevated EKE values, most notably downstream of Denmark Strait. The elevated baroclinic production in that particular region actually takes place near the

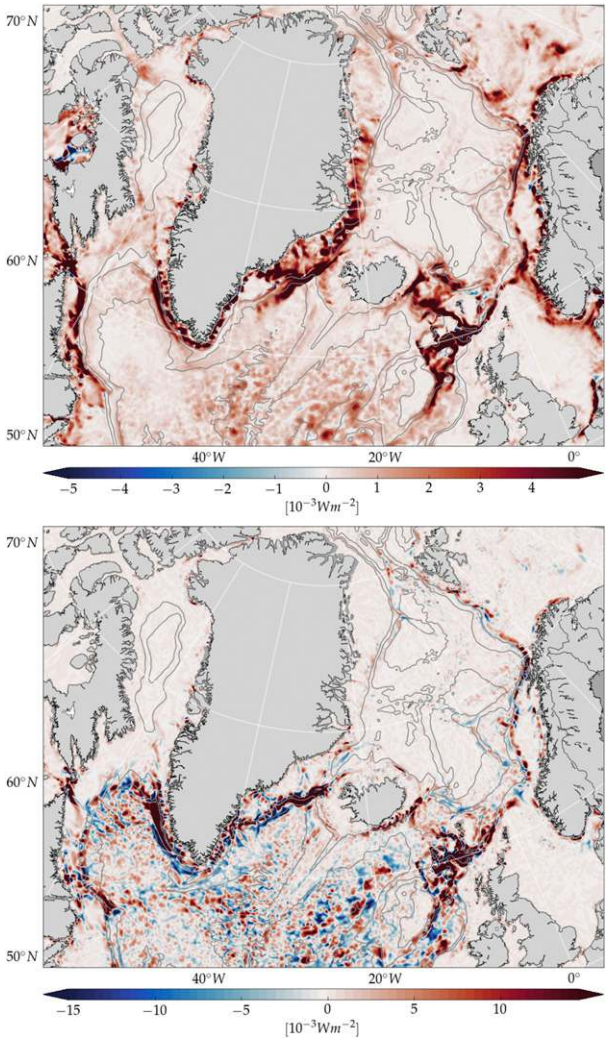

FIG. 4. (top) Depth-integrated MAPE-to-EAPE conversion T_2 and (bottom) MKE-to-EKE conversion T_4 ($10^{-3}\,\mathrm{W\,m^{-2}}$) from diagnosed model Reynolds fluxes.

bottom and involves dense waters that spill over the strait (Jungclaus et al. 2001; Mastropole et al. 2017). So whereas this process is not well captured by the surface EKE (Figs. 2 and 3), it does show up in bottom EKE densities (not shown).

The barotropic production term T_4, related to barotropic instability, is shown in the bottom panel of Fig. 4. This estimate is more noisy, displaying rapidly alternating regions of positive and negative values. But a first impression is that that barotropic instability ($T_4 > 0$) is also taking place along the boundary currents and may, in some places, dominate over baroclinic instability. This impression may partly be an artifact stemming from our choice of using a local rather than a globally averaged N^2 in the computation of T_2 (a globally averaged N^2, which also integrates over the weakly stratified interior basins, would be smaller than the local values over the highly stratified boundary currents). But a pronounced positive T_4 region off the southwest coast of Greenland is consistent with the claim by Eden and Böning (2002) that Irminger rings are formed by barotropic instability here. Positive T_4 along the Irminger rings formation site has also been reported by other studies (Zhu et al. 2014; Chen et al. 2014). So barotropic instability is likely also a ubiquitous process along the boundary currents in these regions, including the Nordic seas (Teigen et al. 2010; Ghaffari et al. 2018). But for the rest of this study we will examine the role of baroclinic instability and the effect the steep continental slopes have on this process.

b. *The characteristics of linear baroclinic instability*

1) Overview and comparison with Eady theory

The linear vertical mode problem was solved at each model grid point using time-mean currents and hydrography. Figure 5 shows the geographic distribution of the growth rate ω_i and corresponding wavelength $L_i = 2\pi/(k^2 + l^2)^{1/2}$ of the fastest-growing unstable modes. Overall, the boundary current regions and the frontal zone along the Greenland–Scotland ridge are the most unstable. Growth in the interior basins is slower, reflecting weaker baroclinic shears there. The agreement with the baroclinic production term T_2 diagnosed from the nonlinear model fields (Fig. 4) is surprisingly good given that this is an estimate based on the low-amplitude QG assumption.

The map of spatial scales of the fastest-growing waves is more noisy than that of growth rates, but some distinct patterns stand out. The stratified branches of the North Atlantic Current (NAC) in the northeastern Atlantic, as well as parts of the NwAC in the eastern Nordic seas and the EGC in the west, depict the largest length scales, reflecting highly stratified waters and large deformation radii there. Scales are smaller in the shallow North Sea and Barents Sea as well as in several of the deep but convective basins, likely reflecting smaller internal deformation radii there. The correspondence with the size of detected vortices (Fig. 3) is not nearly as clear as that between growth rates and baroclinic production T_2. But we note that the linear calculation does pick up the suppression of length scales along most continental slope regions, which is also seen in the fully developed turbulent field. We take this agreement as evidence that topographic slopes impact the mesoscale dynamics to the lowest order in these ocean regions—both for linear growth of baroclinic instability and for finite-amplitude eddies.

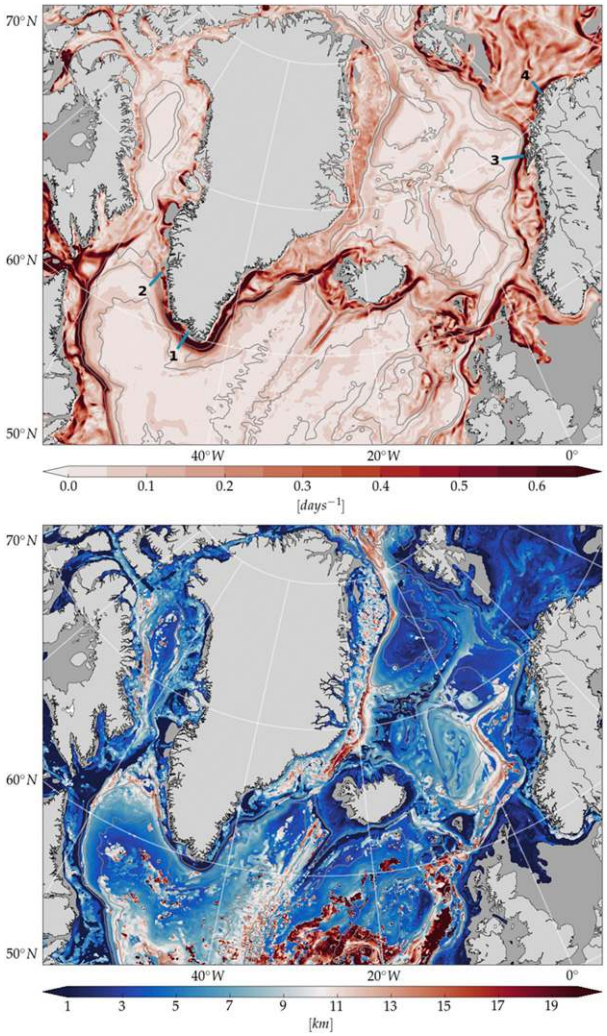

FIG. 5. (top) Growth rates (days^{-1}) and (bottom) wavelength (km) of the fastest-growing mode at each grid point. Areas shallower than 100 m have been masked out (in gray). In (a), we have also shown four transects discussed later in the text.

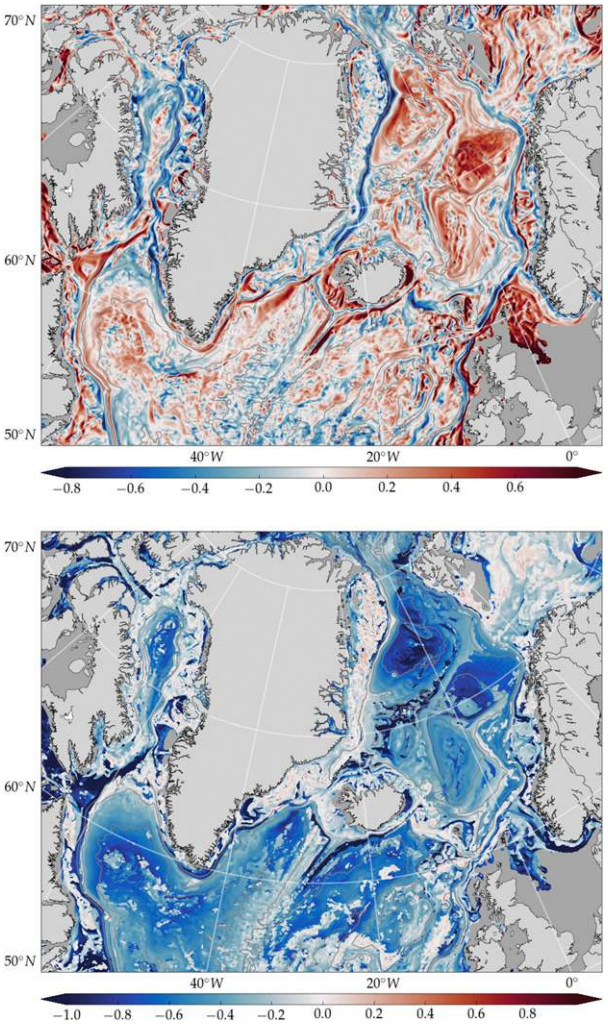

FIG. 6. (top) Growth rates and (bottom) wavelengths normalized by the corresponding values from Eady theory. Logarithmic color scales have been used, and areas shallower than 100 m have been masked out (in gray).

In summary, the linear growth calculations suggest the most intense mesoscale development to occur over the topographic slopes—in agreement with our diagnosis of the EAPE production term T_2. That the slope regions are the most unstable seems intuitive since density fronts are the sharpest there. But as also outlined above, Eady theory modified to include topography (Blumsack and Gierasch 1972; Mechoso 1980) predicts that unstable growth over the continental slope should be *reduced* relative to the corresponding values for flat-bottom conditions. To look for indication of such topographic suppression, growth rates and length scales normalized by the corresponding predictions from flat-bottom Eady theory have therefore been plotted in Fig. 6. We see that many slope regions are indeed characterized by lower normalized growth rates and shorter normalized length scales. The calculation, however, also shows regions with growth rates up to an order of magnitude higher than that of flat-bottom Eady dynamics, a result that is not predicted by the modified theory of Blumsack and Gierasch (1972). So modified Eady theory seems to account, qualitatively, for the observed growth at some locations but not all. Eady theory, whether it accounts for a bottom slope or not, is of course extremely limited in scope since it neglects the effects of internal PV gradients. The use of the full vertical QG modal equations, as done here, allows us a better chance of seeing how topography affects instability. The key to such understanding is the vertical structure of the PV gradient and specifically,

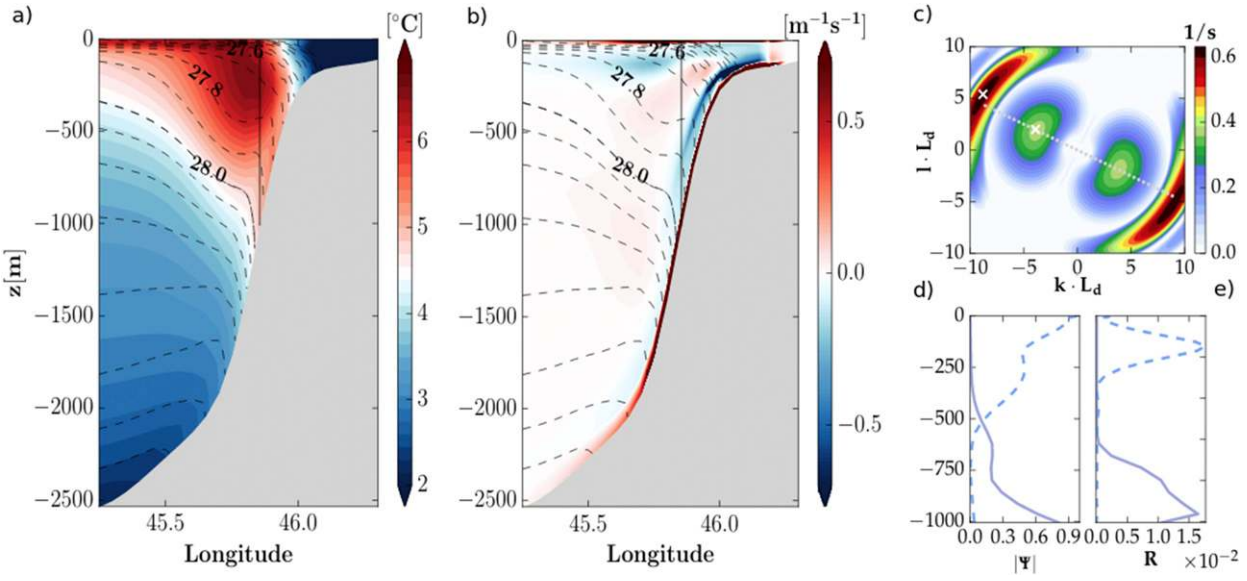

FIG. 7. Stability properties at a location off the southwestern coast of Greenland (location 1 in Fig. 5). Vertical sections of (a) time-mean temperature (°C) and (b) time-mean lateral PV gradient ($m^{-1}s^{-1}$), (c) growth rates ($days^{-1}$) as a function of nondimensional wavenumbers, and vertical profiles of (d) perturbation streamfunction amplitude ($m^2 s^{-1}$) and (e) baroclinic energy conversion rate $R_{MAPE \to EAPE}$ (10^{-3} W m^{-3}) of the two most unstable waves (solid and dashed lines for the first and second modes, respectively).

as discussed below, the location of zero crossings in such gradients.

2) THE VERTICAL STRUCTURE OF UNSTABLE MODES

In this section we look in more detail at the vertical structure of background internal PV gradients and perturbation pressure of the fastest-growing waves at four locations (indicated by numbers in Fig. 5). The hope is to gain some understanding of the nature of instability and thereby check the extent to which Eady dynamics—with or without a bottom slope—offers a useful description of unstable growth.

We start by exploring a profile situated off the southern coast of Greenland, at 59.49°N, 45.59°W. Figure 7a shows a time-mean temperature transect through the site (line 1 in Fig. 5), taken perpendicular to the continental slope. The West Greenland Current (WGC), an extension of the EGC that resides on the shelf, carries cold and fresh surface water originating from the Arctic Ocean and from Greenland runoff. The Irminger Current (IC) is located farther offshore and carries recirculated warm, saline Atlantic water (Katsman et al. 2004). The juxtaposition of these water masses sets up a strong cross-shore density gradient resulting in inclined isopycnals with associated near-surface currents in thermal wind balance. Clearly, the tilted isopycnals reflect a large reservoir of APE that can be extracted by instability.

Isopycnal slopes at this location also steepen drastically near the bottom. This is likely the result of downslope bottom Ekman transport from the nortwestward-flowing currents. The flow in the EGC and WGC extends to all the way to the bottom, exporting dense deep waters produced north of the Greenland–Scotland Ridge. So the bottom flow is nonzero, and buoyant water from the shelf is likely advected down the slope in Ekman layers, raising APE. The process would ultimately be halted by convective overturning if isopycnals become vertical, but it can also be halted at an earlier stage by baroclinic instability. In fact, Brink (2016) suggests that such a balance between near-bottom Ekman transport and bolus transport by baroclinic instability may be an important source of small-scale eddies over continental shelves in general.

Figure 7b shows lateral PV gradient $\nabla(\beta y + \Gamma\Psi)$ along the transect. The gradient is taken in a rotated right-handed coordinate system with the x axis aligned along the wave vector of the unstable wave, which for these cases translates to the horizontal direction of the thermal wind shear vector. Clearly, the PV gradient is not zero in the interior water column, as assumed by Eady theory. Over large parts of the slope the gradient changes sign twice in the vertical, suggesting that at least two distinct unstable modes may be present. Indeed, a plot of growth rates estimated halfway up the slope as a function of wavenumber (Fig. 7c) reveals at least two modes, both aligned with the top-to-bottom thermal wind shear. The fastest-growing mode has a horizontal length scale of approximately $L_d/8$ (cf. $L_d/1.6$ for flat-bottom Eady), and the vertical structure of the perturbation

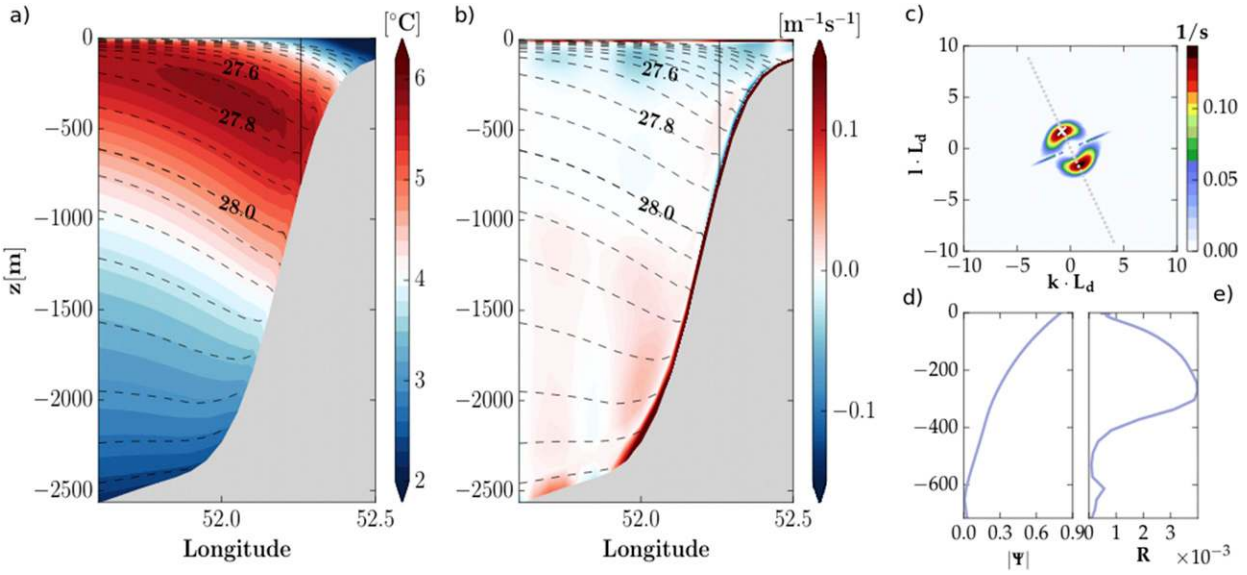

FIG. 8. As in Fig. 7, but for location 2 farther northwest along the south Greenland continental slope.

streamfunction (Fig. 7d) reveals that this mode is bottom intensified. The mode is associated with the lower of the two PV-gradient zero crossings and stems from an interaction between PV anomalies near the bottom and in the interior.

The EAPE production per unit volume (i.e., T_2 per unit depth) is

$$R_{\mathrm{MAPE}\to\mathrm{EAPE}} = -\rho_0 \overline{\mathbf{u}b} \cdot \frac{\nabla B}{N^2}, \tag{14}$$

where the overline here is the time mean, which has also been used to define the background field. In the QG formalism this becomes (Gill et al. 1974; Smith 2007)

$$R_{\mathrm{MAPE}\to\mathrm{EAPE}} = -\rho_0 \frac{f^2}{N^2} \overline{\nabla\psi \frac{\partial\psi}{\partial z}} \cdot \frac{\partial \mathbf{U}}{\partial z}. \tag{15}$$

Absolute extraction rates from any given mode depend on the unknown magnitude of the perturbation streamfunction (i.e., on the equilibrated EKE level). But the expression can tell us where in the water column MAPE is extracted. The result (Fig. 7e) shows maximum energy extraction near the bottom. The mode, apparently, works to flatten the very steep isopycnals near the bottom set up by the downslope bottom Ekman transport.

The second growing mode displays completely different vertical characteristics. It is surface intensified but with larger scales both in the vertical and horizontal (approximately $L_d/3$). The maximum energy conversion rate of this mode is found approximately where the background PV gradient changes sign at around 200 m and apparently works to flatten the density front separating WGC and IC waters.

The same two archetypal modes are commonly found along the entire southern coast of Greenland, where very fresh and buoyant water resides on the shelf slope. But farther west, where the continental slope widens and the isobaths start to turn southward, the hydrography, background PV gradient, and growth characteristics become different. An example from 62.94°N, 52.25°W is shown in Fig. 8 (line 2 in Fig. 5). Both waters associated with the WGC and IC are present here too, but lateral density gradients are weaker and, importantly, the steepening of isopycnals near the bottom is absent. The bottom flow is very weak here, and the result is a very weak downslope Ekman transport. As a consequence there is only one PV gradient reversal in the water column and only one unstable mode. This mode is surface intensified but deep, decaying very gradually to a value of zero at the bottom. Since the mode is deep, horizontal scales are larger than farther east, around $L_d/2$.

Although the unstable mode is deep, there is clear indication that Eady dynamics is not at play. The Eady model involves interacting edge waves and the perturbation streamfunction therefore attains its highest magnitude at the top and bottom boundary. But here, as for the surface mode at the location farther south, the unstable mode attains zero amplitude at the bottom. So a lower boundary edge wave is not at play. Instability might rather occur through an interaction between a surface edge wave and an internal PV wave or, alternatively, an interaction between two internal PV waves.

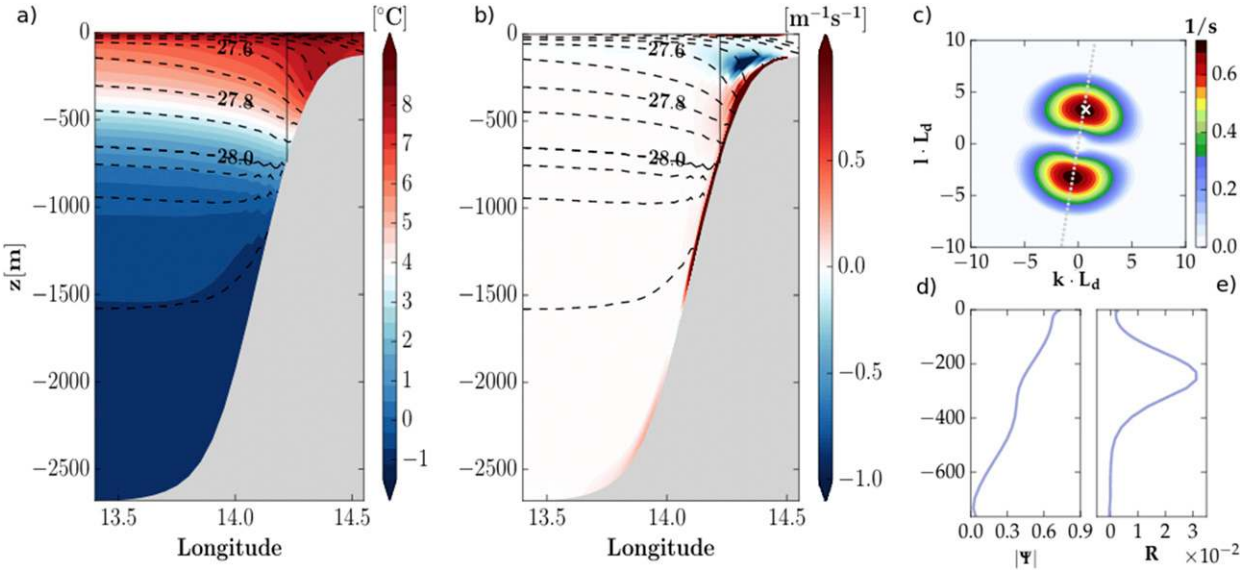

FIG. 9. As in Fig. 7, but for location 3 off the north Norwegian coast.

This situation (i.e., a growing mode that is deep but surface intensified, attaining zero amplitude at the bottom), is rather common along the continental slopes in our study region. Figure 9 shows another example from off the north Norwegian coast east of the Lofoten Basin (line 3 in Fig. 5). Here too the mode appears to involve interactions between a surface edge wave and an internal PV wave that act to flatten isopycnals over large parts of the water column while shutting off at the very bottom. It is worth noting that by attaining zero amplitude at depth the mode is essentially unaffected by the topographic PV gradient.

So over most of the continental slope, Eady theory seems not to apply. Bottom edge waves are for the most part not participating in the unstable interactions and internal Rossby waves, feeding on internal PV gradients, are instead needed. Evidence of pure Eady growth can only be found in a few places, notably where bottom slopes are weak. We include an example from a location in the Barents Sea at 72.47°N, 23.44°E (line 4 in Fig. 5). Figure 10 displays

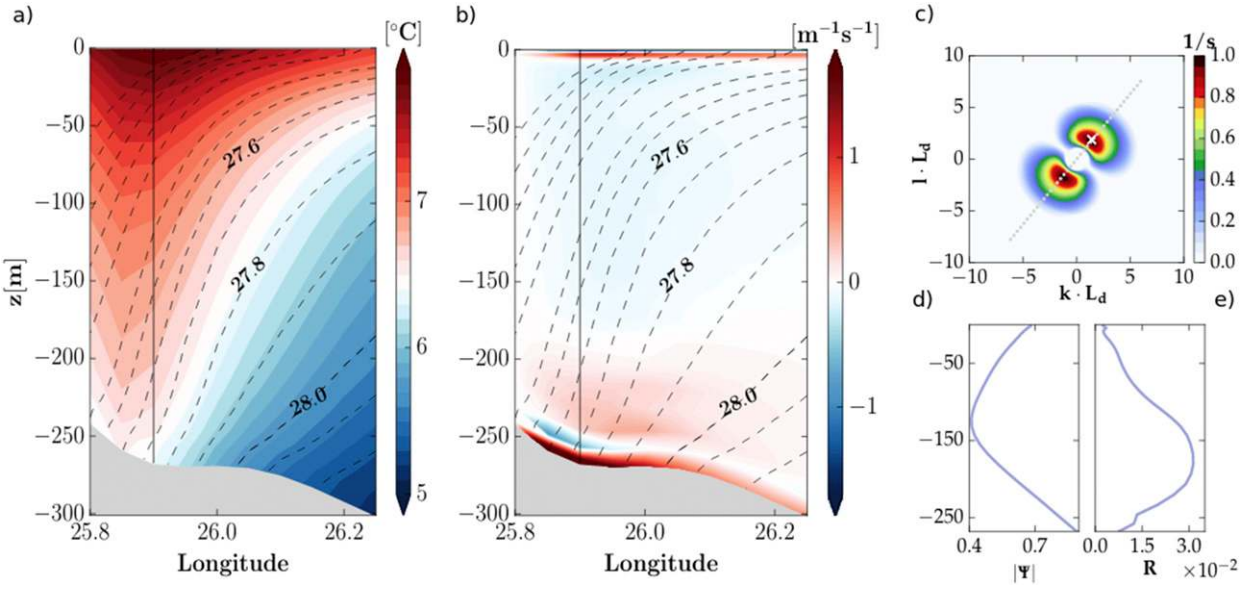

FIG. 10. As in Fig. 7, but for location 4 in the Barents Sea.

the hydrography and stability characteristics there. The largest growth rates occur at a scale of approximately $L_d/2.5$, and the wave is aligned with the thermal wind shear. Moreover, the perturbation pressure amplitude is minimum at middepths and increasing toward both boundaries, consistent with Eady dynamics. The perturbation pressure is also slightly larger at the bottom boundary than at the top, consistent with modified Eady theory with a negative slope parameter δ (see Fig. 6 of Isachsen 2015).

4. Summary and conclusions

The stability of currents in the northwestern North Atlantic and Nordic seas has been studied in isolated spots in the past. But here we looked at the overall geography of baroclinic instability and its relationship to the macroturbulent flow field in this region for the first time. Unsurprisingly, the calculations indicate that the currents are baroclinically unstable all along the continental slopes and also along underwater ridge systems. In a few locations, notably off the south Greenland coast, the fastest-growing waves are bottom intensified, acting to flatten steep isopycnals near the bottom. But for the most part instability works to release available potential energy associated with buoyant boundary currents residing at the surface.

We have seen that the steepest parts of the continental slopes generally have both the highest EKE levels and the fastest conversion of MAPE to EAPE. We also found that currents over the steep slopes are, for the most part, also the most baroclinically unstable—according to the linear QG vertical mode calculations conducted here. Of course the QG linear stability analysis has many limitations, the most severe of which are probably the small-slope assumption and the assumption of homogeneous conditions over the scale of the unstable waves. The validity of both assumptions become more questionable as the horizontal resolution of the analysis is increased. For example, the hydrographic and flow structure across the continental slopes in this region changes over a few tens of kilometers whereas the unstable waves we find have scales of a few kilometers. So the slowly changing background field assumption is not fulfilled in a strict sense. Furthermore, it is clear that the smallest scales predicted by the linear theory will not be resolved by the 4-km ROMS model or detected by our vortex detection algorithm with its detection threshold of 8 km. Finally, at scales of a few kilometers quasi geostrophy itself becomes questionable. A Rossby number cannot be estimated from the linear model results since these do not give a velocity scale. But if we assume that linear growth eventually leads to fully developed eddies of strength $10\,\mathrm{cm\,s^{-1}}$ and scale 2 km, an effective Rossby number would be around 0.5. So one should be skeptical of the quantitative predictions of the linear growth estimates, particularly with respect to the smallest scales. Nevertheless, the impressive qualitative match between the obtained maps of baroclinic production T_2 and linear growth rate (Figs. 4 and 5) leads us to believe that there is ample qualitative information in these vertical mode QG calculations.

That unstable growth should be highest over the steepest continental slopes, as observed in most places here, is seemingly in contradiction with the modified Eady theory of Blumsack and Gierasch (1972) and Mechoso (1980). The theory predicts lower growth rates for nonflat topography—for the same thermal wind shear. Spall (2010) offers the explanation that in freely evolving flows the isopycnal slope of a boundary current adjusts continuously to the underlying bottom topography so that the slope parameter δ remains constant. So nondimensional growth rates will be constant regardless of the shape of the bottom underneath and steep slope regions will have higher *absolute* growth rates caused by a stronger thermal wind shear. This is essentially the ''baroclinic adjustment'' argument of Stone (1978) that macroturbulent transport is so effective that it keeps the criticality of the flow with respect to large-scale PV gradients (here being set by bottom topography) constant.

An alternative explanation has been proposed in relation to what takes place along the southwestern continental slope of Greenland. Here Bracco and Pedlosky (2003) and Bracco et al. (2008) suggested that a very steep slope basically acts as a vertical wall such that part of the mean flow really feels a flat bottom underneath. This notion was qualitatively supported in laboratory tank experiments by Wolfe and Cenedese (2006). They found the most important parameter in determining instability to be the width of the current relative to the width of the bottom slope region. Where the baroclinic current was narrower than the slope region underneath the flow was stabilized. But when the same current was made to flow over a very narrow slope—so that part of the current felt a flat bottom—it immediately became unstable.

Here we have pointed to an additional factor that may be at play. What we have seen is a general tendency for suppressed length scales over the continental slopes, a suppression that is related to a shortening of the vertical scale of instabilities. Around the southern tip of Greenland we have found bottom-trapped instabilities, but more generally we see instabilities that have zero amplitude at the bottom over steep slopes. This is clearly inconsistent with Eady dynamics, which relies on

interacting top and bottom edge waves. As discussed by Isachsen (2015), the flow field instead appears to organize itself so as to shelter the instability from the topographic PV gradients, which generally inhibits unstable growth. It is worth mentioning that de La Lama et al. (2016), in studying current meter records from all over the World Oceans, frequently found leading vertical empirical modes (EOFs) that have zero amplitude at the bottom. Motivated by this observational result LaCasce (2017) has argued that topographic slopes in the real oceans are nearly everywhere large enough to prevent the textbook flat-bottom baroclinic modes from existing. He instead advocates that steep-slope or ''rough bottom'' baroclinic modes are the orthogonal modes that should be used to characterize free waves. Our study here suggests that this result extends qualitatively over to baroclinically unstable waves as well, at least in the northern North Atlantic.

So at least three explanations have been proposed for why the boundary currents in the northern North Atlantic are generally more unstable over the steepest continental slopes. Untangling these explanations will require further effort, likely involving idealized modeling of freely evolving flows over a range topographic variations and forcing strengths (e.g., to examine the baroclinic adjustment hypothesis). An acceptable lowest-order theory must also be able to account for the few regions where unstable growth is *not* enhanced over the continental slope (e.g., as seen along northeastern Greenland in Fig. 5). Here we wish to emphasize that the surface-intensified (and in some cases bottom intensified) structure of unstable waves strongly suggest that instability be formed by interaction between surface edge waves and internal PV waves or entirely between internal PV waves, rather than between top and bottom edge waves. So the Eady model and two-layer Phillips models are clearly insufficient lowest-order descriptions whether they take a bottom slope into account or not. We believe that a three-layer model—with its ability to include an internal PV gradient reversal—is the minimal description required to get these processes right. This is not only important for our conceptual understanding but has implications for how eddy transport should be parameterization in coarse-grained climate models. The added complexity of one additional layer to the classical two-layer description seems daunting. But we believe it will be necessary if one wishes to obtain an adequate representation of topographic effects on mesoscale ocean dynamics and transport in these high-latitude regions.

Acknowledgments. The work was partially funded by Grant 221780 from the Research Council of Norway. The dynamic ocean topography fields used were produced by CLS Space Oceanography Division and distributed by AVISO, with support from CNES (http://www.aviso.altimetry.fr/).

REFERENCES

Aaboe, S., and O. A. Nøst, 2008: A diagnostic model of the Nordic seas and Arctic Ocean circulation: Quantifying the effects of a variable bottom density along a sloping topography. *J. Phys. Oceanogr.*, **38**, 2685–2703, https://doi.org/10.1175/2008JPO3862.1.

Aiki, H., X. Zhai, and R. J. Greatbatch, 2016: Energetics of the global ocean: The role of mesoscale eddies. *Indo-Pacific Climate Variability and Predictability*, S. Behera and T. Yamagata, Eds., World Scientific Series on Asia-Pacific Weather and Climate, Vol. 7, World Scientific, 109–134, https://doi.org/10.1142/9789814696623_0004.

Blumsack, S. L., and P. J. Gierasch, 1972: Mars: The effects of topography on baroclinic instability. *J. Atmos. Sci.*, **29**, 1081–1089, https://doi.org/10.1175/1520-0469(1972)029<1081:MTEOTO>2.0.CO;2.

Bracco, A., and J. Pedlosky, 2003: Vortex generation by topography in locally unstable baroclinic flows. *J. Phys. Oceanogr.*, **33**, 207–219, https://doi.org/10.1175/1520-0485(2003)033<0207:VGBTIL>2.0.CO;2.

——, ——, and R. S. Pickart, 2008: Eddy formation near the west coast of Greenland. *J. Phys. Oceanogr.*, **38**, 1992–2002, https://doi.org/10.1175/2008JPO3669.1.

Brink, K. H., 2016: Continental shelf baroclinic instability. Part I: Relaxation from upwelling or downwelling. *J. Phys. Oceanogr.*, **46**, 551–568, https://doi.org/10.1175/JPO-D-15-0047.1.

Chanut, J., B. Barnier, W. Large, L. Debreu, T. Penduff, J. M. Molines, and P. Mathiotc, 2008: Mesoscale eddies in the Labrador Sea and their contribution to convection and restratification. *J. Phys. Oceanogr.*, **38**, 1617–1643, https://doi.org/10.1175/2008JPO3485.1.

Chelton, D. B., M. G. Schlax, R. M. Samelson, and R. A. de Szoeke, 2007: Global observations of large oceanic eddies. *Geophys. Res. Lett.*, **34**, L15606, https://doi.org/10.1029/2007GL030812.

Chen, R., G. R. Flierl, and C. Wunsch, 2014: A description of local and nonlocal eddy-mean flow interaction in a global eddy-permitting state estimate. *J. Phys. Oceanogr.*, **44**, 2336–2352, https://doi.org/10.1175/JPO-D-14-0009.1.

de Jong, M. F., A. S. Bower, and H. H. Furey, 2014: Two years of observations of warm-core anticyclones in the Labrador Sea and their seasonal cycle in heat and salt stratification. *J. Phys. Oceanogr.*, **44**, 427–444, https://doi.org/10.1175/JPO-D-13-070.1.

de La Lama, M. S., J. H. LaCasce, and H. K. Fuhr, 2016: The vertical structure of ocean eddies. *Dyn. Stat. Climate Syst.*, **1**, dzw001, https://doi.org/10.1093/climsys/dzw001.

Donlon, C. J., M. Martin, J. Stark, J. Roberts-Jones, E. Fiedler, and W. Wimmer, 2012: The Operational Sea Surface Temperature and Sea Ice Analysis (OSTIA) system. *Remote Sens. Environ.*, **116**, 140–158, https://doi.org/10.1016/j.rse.2010.10.017.

Eden, C., and C. Böning, 2002: Sources of eddy kinetic energy in the Labrador Sea. *J. Phys. Oceanogr.*, **32**, 3346–3363, https://doi.org/10.1175/1520-0485(2002)032<3346:SOEKEI>2.0.CO;2.

Gelderloos, R., C. A. Katsman, and S. S. Drijfhout, 2011: Assessing the roles of three eddy types in restratifying the Labrador Sea after deep convection. *J. Phys. Oceanogr.*, **41**, 2102–2119, https://doi.org/10.1175/JPO-D-11-054.1.

Ghaffari, P., P. E. Isachsen, O. A. Nøst, and J. E. Weber, 2018: The influence of topography on the stability of the Norwegian Atlantic Current off northern Norway. *J. Phys. Oceanogr.*, https://doi.org/10.1175/JPO-D-17-0235.1, in press

Gill, A., J. Green, and A. Simmons, 1974: Energy partition in the large-scale ocean circulation and the production of mid-ocean eddies. *Deep-Sea Res.*, **21**, 499–528, https://doi.org/10.1016/0011-7471(74)90010-2.

Haidvogel, D., and Coauthors, 2008: Ocean forecasting in terrain-following coordinates: Formulation and skill assessment of the Regional Ocean Modeling System. *J. Comput. Phys.*, **227**, 3595–3624, https://doi.org/10.1016/j.jcp.2007.06.016.

Haney, R. L., 1991: On the pressure gradient force over steep topography in sigma coordinate ocean models. *J. Phys. Oceanogr.*, **21**, 610–619, https://doi.org/10.1175/1520-0485(1991)021<0610:OTPGFO>2.0.CO;2.

Hátún, H., C. C. Eriksen, and P. B. Rhines, 2007: Buoyant eddies entering the Labrador Sea observed with gliders and altimetry. *J. Phys. Oceanogr.*, **37**, 2838–2854, https://doi.org/10.1175/2007JPO3567.1.

Isachsen, P. E., 2011: Baroclinic instability and eddy tracer transport across sloping bottom topography: How well does a modified Eady model do in primitive equation simulations? *Ocean Modell.*, **39**, 183–199, https://doi.org/10.1016/j.ocemod.2010.09.007.

——, 2015: Baroclinic instability and the mesoscale eddy field around the Lofoten Basin. *J. Geophys. Res. Oceans*, **120**, 2884–2903, https://doi.org/10.1002/2014JC010448.

——, J. H. LaCasce, C. Mauritzen, and S. Häkkinnen, 2003: Wind-driven variability of the large-scale recirculating flow in the Nordic seas and Arctic Ocean. *J. Phys. Oceanogr.*, **33**, 2534–2550, https://doi.org/10.1175/1520-0485(2003)033<2534:WVOTLR>2.0.CO;2.

Isern-Fontanet, J., E. García-Ladona, and J. Font, 2003: Identification of marine eddies from altimetric maps. *J. Atmos. Oceanic Technol.*, **20**, 772–778, https://doi.org/10.1175/1520-0426(2003)20<772:IOMEFA>2.0.CO;2.

Jungclaus, J. H., J. Hauser, and R. H. Käse, 2001: Cyclogenesis in the Denmark Strait overflow plume. *J. Phys. Oceanogr.*, **31**, 3214–3229, https://doi.org/10.1175/1520-0485(2001)031<3214:CITDSO>2.0.CO;2.

Katsman, C. A., M. A. Spall, and R. S. Pickart, 2004: Boundary current eddies and their role in the restratification of the Labrador Sea. *J. Phys. Oceanogr.*, **34**, 1967–1983, https://doi.org/10.1175/1520-0485(2004)034<1967:BCEATR>2.0.CO;2.

LaCasce, J. H., 2017: The prevalence of oceanic surface modes. *Geophys. Res. Lett.*, **44**, 11 097–11 105, https://doi.org/10.1002/2017GL075430.

——, and K. Brink, 2000: Geostrophic turbulence over a slope. *J. Phys. Oceanogr.*, **30**, 1305–1324, https://doi.org/10.1175/1520-0485(2000)030<1305:GTOAS>2.0.CO;2.

Le Traon, P. Y., M. C. Rouquet, and C. Boissier, 1990: Spatial scales of mesoscale variability in the North Atlantic as deduced from Geosat data. *J. Geophys. Res.*, **95**, 20 267–20 285, https://doi.org/10.1029/JC095iC11p20267.

Lilly, J. M., P. B. Rhines, F. Schott, K. Lavender, J. Lazier, U. Send, and E. D. Asaro, 2003: Observations of the Labrador Sea eddy field. *Prog. Oceanogr.*, **59**, 75–176, https://doi.org/10.1016/j.pocean.2003.08.013.

Lorenz, E. N., 1955: Available potential energy and the maintenance of the general circulation. *Tellus*, **7A**, 157–167, https://doi.org/10.1111/j.2153-3490.1955.tb01148.x.

MacLachlan, C., and Coauthors, 2015: Global Seasonal forecast system version 5 (GloSea5): A high-resolution seasonal forecast system. *Quart. J. Roy. Meteor. Soc.*, **141**, 1072–1084, https://doi.org/10.1002/qj.2396.

Mastropole, D., R. S. Pickart, H. Valdimarsson, K. Våge, K. Jochumsen, and J. Girton, 2017: On the hydrography of Denmark Strait. *J. Geophys. Res. Oceans*, **122**, 306–321, https://doi.org/10.1002/2016JC012007.

Mechoso, C. R., 1980: Baroclinic instability of flows along sloping boundaries. *J. Atmos. Sci.*, **37**, 1393–1399, https://doi.org/10.1175/1520-0469(1980)037<1393:BIOFAS>2.0.CO;2.

Nøst, O. A., and P. E. Isachsen, 2003: The large-scale time-mean ocean circulation in the Nordic seas and Arctic Ocean estimated from simplified dynamics. *J. Mar. Res.*, **61**, 175–210, https://doi.org/10.1357/002224003322005069.

Penven, P., V. Echevin, J. Pasapera, F. Colas, and J. Tam, 2005: Average circulation, seasonal cycle, and mesoscale dynamics of the Peru Current System: A modeling approach. *J. Geophys. Res.*, **110**, C10021, https://doi.org/10.1029/2005JC002945.

Shchepetkin, A. F., and J. C. McWilliams, 2005: The Regional Oceanic Modeling System (ROMS): A split-explicit, free-surface, topography-following-coordinate oceanic model. *Ocean Modell.*, **9**, 347–404, https://doi.org/10.1016/j.ocemod.2004.08.002.

Smith, K. S., 2007: The geography of linear baroclinic instability in Earth's oceans. *J. Mar. Res.*, **65**, 655–683, https://doi.org/10.1357/002224007783649484.

Spall, M. A., 2010: Non-local topographic influences on deep convection: An idealized model for the Nordic seas. *Ocean Modell.*, **32**, 72–85, https://doi.org/10.1016/j.ocemod.2009.10.009.

Stone, P. H., 1978: Baroclinic adjustment. *J. Atmos. Sci.*, **35**, 561–571, https://doi.org/10.1175/1520-0469(1978)035<0561:BA>2.0.CO;2.

Teigen, S. H., F. Nilsen, and B. Gjevik, 2010: Barotropic instability in the West Spitsbergen Current. *J. Geophys. Res.*, **115**, C07016, https://doi.org/10.1029/2009JC005996.

Umlauf, L., and H. Burchard, 2003: A generic length-scale equation for geophysical turbulence models. *J. Mar. Res.*, **61**, 235–265, https://doi.org/10.1357/002224003322005087.

Uppala, S. M., and Coauthors, 2005: The ERA-40 Re-Analysis. *Quart. J. Roy. Meteor. Soc.*, **131**, 2961–3012, https://doi.org/10.1256/qj.04.176.

Vallis, G. K., and M. E. Maltrud, 1994: Generation of mean flows and jets on a beta plane and over topography. *J. Phys. Oceanogr.*, **23**, 1346–1362, https://doi.org/10.1175/1520-0485(1993)023<1346:GOMFAJ>2.0.CO;2.

Vollmer, L., and K. Eden, 2013: A global map of meso-scale eddy diffusivities based on linear stability analysis. *Ocean Modell.*, **72**, 198–209, https://doi.org/10.1016/j.ocemod.2013.09.006.

von Storch, J.-S., C. Eden, I. Fast, H. Haak, D. Hernández-Deckers, E. Maier-Reimer, J. Marotzke, and D. Stammer, 2012: An estimate of the Lorenz energy cycle for the World Ocean based on the STORM/NCEP simulation. *J. Phys. Oceanogr.*, **42**, 2185–2205, https://doi.org/10.1175/JPO-D-12-079.1.

Warner, J. C., C. R. Sherwood, H. G. Arango, and R. P. Signell, 2005: Performance of four turbulence closure models implemented using a generic length scale method. *Ocean Modell.*, **8**, 81–113, https://doi.org/10.1016/j.ocemod.2003.12.003.

Wolfe, C. L., and C. Cenedese, 2006: Laboratory experiments of eddy generation by a buoyant coastal current flowing over variable bathymetry. *J. Phys. Oceanogr.*, **36**, 395–411, https://doi.org/10.1175/JPO2857.1.

Zhu, J. S., E. Demirov, Y. Zhang, and A. Polomska-Harlick, 2014: Model simulations of mesoscale eddies and deep convection in the Labrador Sea. *Adv. Atmos. Sci.*, **31**, 743–754, https://doi.org/10.1007/s00376-013-3107-y.